PAPER

Check for updates

Outstanding MRI contrast with dysprosium phosphate nanoparticles of tuneable size†

Elisabet Gómez-González, [a] Carlos Caro, [b] María L. García-Martín, [b]
Ana Isabel Becerro *[a] and Manuel Ocaña [a]

The use of high-field magnets for magnetic resonance imaging (MRI) is expected to experience the fastest growth rate during the present decade. Although several CAs for MRI scanners using high magnetic fields have been reported, they are mostly based on fluoride matrices, which are known for their low chemical stability in aqueous suspensions. Chemically stable MRI CAs for high-field magnets are therefore needed to enable the advances in MRI technique. Herein, we synthesized uniform $DyPO_4$ nanoparticles (NPs) with tuneable sizes between 23 and 57 nm using homogeneous precipitation in butanol. The NPs were successfully functionalized with polyacrylic acid (PAA) and showed good colloidal stability in aqueous suspensions. Chemical stability was also assessed in PBS, showing negligible solubility. The effect of particle size on the transversal relaxivity value (r_2) was further explored at 9.4 T, finding a clear increase in r_2 with particle size. The r_2 value found for the largest NPs was 516 mM^{-1} s^{-1}, which is, to the best of our knowledge, the highest r_2 value ever reported at 9.4 T for any Dy-based nanometric particles in the literature. Finally, the latter NPs were submitted to biosafety studies after polyethylene glycol (PEG) functionalization. Cell morphology, induction of necrotic/late apoptotic cells, and mitochondrial activity were thoroughly analyzed. The results clearly indicated negligible toxicity effects under the assayed conditions. Short- and long-term *in vivo* pharmacokinetics of the intravenously injected NPs were assessed by dynamic T_2-weighted MRI and quantitative T_2 mapping, revealing faster liver than spleen uptake, while no accumulation was observed in the kidneys. Finally, no histopathological changes were observed in any of the studied organs, including the liver, kidney, spleen, and lung, which provide further evidence of the biocompatibility of $DyPO_4$ NPs and, therefore, their suitability as bioimaging probes.

1. Introduction

Magnetic Resonance Imaging (MRI) is a non-invasive imaging technology that produces three-dimensional detailed anatomical images thanks to the effect of an external magnetic field. It is very often used for biomedical research as well as for disease detection, diagnosis, and treatment monitoring. Compared to other imaging techniques, such as optical imaging, MRI has high spatial resolution but rather low sensitivity. Increasing magnetic field strength (B_0) increases sensitivity and produces, therefore, a higher signal-to-noise ratio with shorter acquisition times. Although the so-called high-field scanners (1.0 T < B_0 < 3.0 T) are the most popular MRI instruments used in clinics nowadays, the very high field (3.0

T < B_0 < 7.0 T) and ultra-high field (UHF) (B_0 > 7.0 T) segments are expected to experience the fastest growth rate during the present decade. In fact, some companies have already developed 7 T MRI machines that are installed in a few hospitals around the world.[1,2] Preliminary MRI studies at 9.4 T in humans were reported as early as 2006,[3] and have been further continued, demonstrating the feasibility of safe and successful human imaging.[4] Even MRI instruments operating at fields as high as 21.1 T are currently being used in preclinical research. Safety studies have demonstrated that static exposure at UHF for 2 h does not have severe long-term effects on mice.[5] The primary goal of UHF systems is to obtain structural and functional information about the brain with the highest possible spatial resolution.

The contrast in MRI images is generated from differences in local water proton density and in the proton relaxation times (T_1 and T_2), which is a magnetic resonance characteristic of protons. In addition to using higher magnetic fields, the contrast in MRI can be further improved through the use of the so-called MRI contrast agents (CAs). MRI CAs are exogenous substances that decrease T_1 and T_2. The capacity of a CA to

[a] Instituto de Ciencia de Materiales de Sevilla (ICMS) CSIC-Universidad de Sevilla, c/ Américo Vespucio, 49, 41092 Seville, Spain. E-mail: anieto@icmse.csic.es
[b] Instituto de Investigación Biomédica de Málaga – Plataforma Bionand (IBIMA-Plataforma BIONAND) and CIBER-BBN, Málaga 29590, Spain
†Electronic supplementary information (ESI) available. See DOI: https://doi.org/10.1039/d2nr02630a

decrease T_1 is known as longitudinal relaxivity (r_1), while its capacity to shorten T_2 is known as transversal relaxivity (r_2). Gadolinium complexes and, to a lesser extent, iron-based CAs are currently used, respectively, as positive and negative CAs in clinics. Both show good contrast at low magnetic fields, but their efficiency drastically decreases at high fields. For example, iron oxide CAs are known to saturate their magnetization at around 1.5 T,[6] while Gd-based CAs present their optimal contrast below 1 T.[7] Suitable CAs for use in UHF MRI scanners are therefore urgently demanded.[8,9]

It is well known that paramagnetic ions other than Gd^{3+}, with fast electronic relaxation rates,[10] relax protons *via* a mechanism known as Curie spin relaxation that primarily affects T_2.[11] Curie-spin relaxation increases substantially with the strength of the magnetic field and is proportional to the square of the magnetic moment of the lanthanide (Ln) ion. Among lanthanides, Dy^{3+} shows the highest magnetic moment value, which has generated a number of studies on the use of Dy-complexes as T_2 CAs for high field MRI.[2,12–16] They exhibit moderate r_2 values at very high (>3.0 T) magnetic fields although they suffer from short blood circulation times. At UHF, these complexes possess low r_2 values, exemplified by Dy-DOTA with r_2 = 10.02 mM^{-1} s^{-1} at 11.7 T (ref. 14) and Dy [EOB-DO3A] with r_2 = 2.67 mM^{-1} s^{-1} at 9.4 T.[15] In contrast to Dy-complexes, several studies on Dy-based inorganic nanoparticles (NPs) have been published showing r_2 values as high as 559.37 mM^{-1} s^{-1} at 9.4 T, which demonstrate their potential as MRI CA at UHF.[17–20] Ln-Based inorganic NPs show an additional and important advantage relative to organic complexes, consisting in their capacity to be surface functionalized. NPs functionalization consists of the attachment of functional groups to the NP surface to confer them with colloidal stability, which is an essential requirement for bioapplications. A frequently used additive for the functionalization of Ln-based NPs is polyacrylic acid (PAA), whose carboxylate groups can also be used as anchors for further binding different molecules. Among them, polyethylene glycol (PEG) is especially interesting as it allows for decreasing immunogenicity and increasing the NPs circulation time.[21] Functionalized NPs can also be conjugated to biological molecules such as antibodies and peptides to provide them with targeting capacity, *i.e.*, the NPs can be specifically directed to the region of interest, thus reducing the dose required.[22] Most of the reported Dy-based inorganic NPs consist of fluoride matrices, which are known to exhibit poor stability in aqueous media,[23,24] leading to the release of potentially toxic fluoride ions. This justifies the search for less soluble alternatives such as Ln-phosphates which show higher chemical stability in water.[25] To the best of our knowledge, the only Dy phosphate-based NPs reported in the literature as MRI CAs are Dy^{3+}-doped β-tricalcium phosphate NPs, with a low content in Dy and correspondingly low r_2 value (3.43 mM^{-1} s^{-1} at 1.5 T),[26] but their relaxivity at high fields is not reported.

In this study, we have synthesized uniform $DyPO_4$ nanoparticles with tuneable sizes from 23 nm to 57 nm. The NPs have been functionalized with polyacrylic acid (PAA) and the colloidal and chemical stability of the resulting NPs in phosphate buffered saline has been analyzed. The ability of the NPs to increase the contrast of MRI images at an ultra-high magnetic field has been evaluated through the measurement of the proton relaxation times in aqueous suspensions of the NPs at 9.4 T. Finally, *in vitro* cytotoxicity, *in vivo* pharmacokinetics, and biodistribution of PAA@PEG functionalized NPs have been studied to assess the suitability of the studied NPs as MRI contrast agents for *in vivo* use.

2. Results

2.1. NPs synthesis, morphology, and crystal phase

TEM micrographs in Fig. 1 show the NPs obtained after aging, at 150 °C for 1 hour in a microwave oven (MW), three butanol solutions containing dysprosium nitrate (0.02 M) and phosphoric acid (0.075 M, 0.15 M, and 0.30 M). All three micrographs showed uniform NPs whose size increased with increasing H_3PO_4 concentration, as observed in the histograms plotted in the same figure. Specifically, the use of very dilute (0.075 M) H_3PO_4 resulted in cube-like NPs with an average value of the face diagonal of 23 nm, while doubling H_3PO_4 concentration to 0.15 M gave also rise to cube-like NPs showing a larger face diagonal size (37 nm). Finally, when the concentration of H_3PO_4 was increased to 0.30 M, more elongated NPs were precipitated with a long axis length of 57 nm. The H_3PO_4 concentration allowed therefore tuning the NPs size from 23 nm to 57 nm while keeping their uniform shape. The NPs shown in Fig. 1 will from now on be called Dy23, Dy37, and Dy57, in reference to their size.

The effect of other experimental parameters such as solvent nature, aging temperature, and heating source on the NPs morphology was subsequently analyzed. Fig. S1† shows the TEM micrographs of the precipitates obtained by changing just one of the experimental conditions used to synthesize the NPs shown in Fig. 1c (Dy37). It can be observed that the solvent nature produced a drastic change in the precipitate obtained, so that using octanol instead of butanol resulted in the precipitation of heterogeneous, fully aggregated tiny NPs (Fig. S1†). Another key factor for the synthesis of uniform NPs was the reaction temperature. When the reaction was carried out at 120 °C (Fig. S1b†) the coexistence of both heterogeneous rods and cubic-like NPs was observed in the reaction product while increasing the temperature to 180 °C gave rise to uniform, cubic-like NPs with ~70 nm edge size (Fig. S1c†). A minimum reaction temperature of 150 °C was, therefore, necessary to obtain homogeneous NPs, while increasing the temperature to 180 °C gave rise to an increase in particle size. Finally, when conventional heating was used instead of MW heating, uniform, cubic-like NPs with ~65 nm edge size were observed (Fig. S1d†). Conventional heating resulted, therefore, in the precipitation of larger particles compared to MW heating. All these changes must be assigned to variations in the kinetics of precipitation which also affect the nucleation and growth processes.[27]
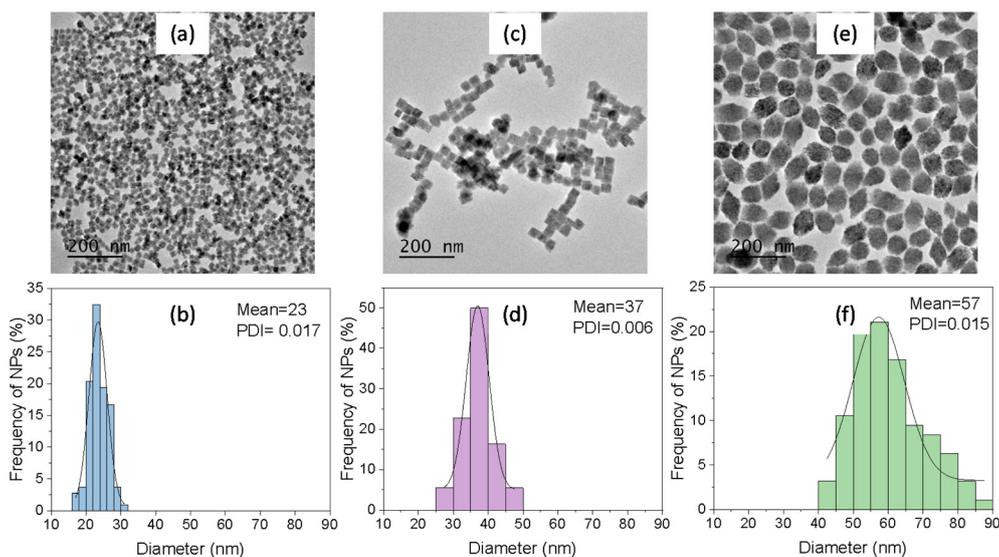
Fig. 1 TEM micrographs and corresponding size distribution histograms of DyPO$_4$ NPs synthesized by solvothermal reaction of butanol solutions of dysprosium nitrate (0.02 M) and different H$_3$PO$_4$ concentrations in a microwave oven at 150 °C for 1 h. [H$_3$PO$_4$] = 0.075 M (a and b, Dy23 NPs), 0.15 M (c and d, Dy37 NPs), 0.30 M (e and f, Dy57 NPs). PDI = Polydispersity index.

The crystal phase of the Dy23, Dy37, and Dy57 NPs was analyzed by XRD (Fig. 2). All three patterns exhibited the same set of reflections, compatible with tetragonal DyPO$_4$ (PDF 00-026-0593). No additional reflections were observed in any of the patterns, indicating the absence of other crystalline phases. It can be noted that the width of the reflections decreased with increasing particle size, indicating that the crystallite size increased correspondingly. The crystallite size was estimated from the half-width at half maximum of the reflection located at ~35° 2θ using the Scherrer formula. Crystallite size values of 26 nm, 34 nm, and 52 nm were obtained for the Dy23, Dy37, and Dy57 NPs, respectively. The value of the crystallite size, very close to the NPs size in each case, suggests that the NPs were single crystals in nature.
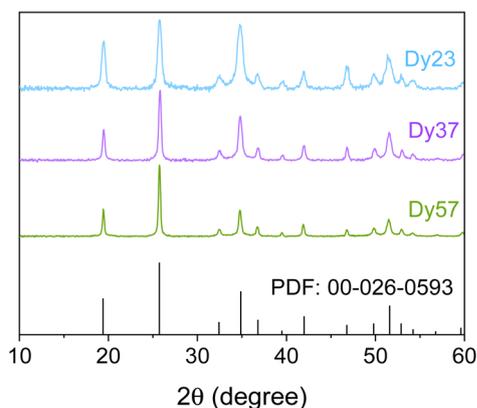

Fig. 2 XRD patterns of Dy23, Dy37, and Dy57 NPs synthesized in the conditions described in Fig. 1. Ticks at the bottom of the figure correspond to tetragonal DyPO$_4$ (PDF 00-026-0593).

2.2. Analysis of the colloidal and chemical stability

The colloidal stability of Dy23 and Dy37 (Fig. S2†) and of Dy57 NPs (Fig. 3a) suspended in water (native pH ∼ 3.5) was evaluated from DLS curves. Mean hydrodynamic diameters of 240 nm, 164 nm, and 142 nm, respectively, were obtained for Dy23, Dy37, and Dy57. These values, higher than the dimensions of the particles obtained from TEM micrographs, indicated that all three types of NPs were aggregated in water. Functionalization of the NPs with PAA was carried out to try to reduce such aggregation. The NPs obtained after such a functionalization process will be called Dy23@PAA, Dy37@PAA, and Dy57@PAA from now on. The success of the functionalization process was monitored through FTIR spectroscopy and thermogravimetry curves. Fig. 3b shows the FTIR spectra of Dy57 NPs before and after PAA coating. The corresponding FTIR spectra of Dy23 and Dy37 NPs are plotted in Fig. S3.† The spectra of the three NPs before functionalization showed the characteristic bands associated with the phosphate vibrational modes (located at wavenumbers <1250 cm^{-1})[28] and adsorbed water (at 3400 cm^{-1} and 1625 cm^{-1}) plus a low-intensity band at around 1400 cm^{-1} (marked with an asterisk) that can be assigned to the presence of residual solvent molecules on the NPs surface. On the other hand, the FTIR spectra of all three NPs after functionalization showed two additional bands at ~1460 cm^{-1} and 1560 cm^{-1} (labeled with arrows) that can be assigned to the vibrations of the carboxylate groups of the PAA molecules.[29] On the other hand, the TG curve of Dy57 NPs before PAA functionalization (Fig. 3c) showed a first weight loss of around 4% at $T < 100$ °C, corresponding to the removal of adsorbed water and a second, progressive one at $T > 100$ °C that could be assigned to the decomposition of the residual solvent molecules. The curve corresponding to the Dy57@PAA
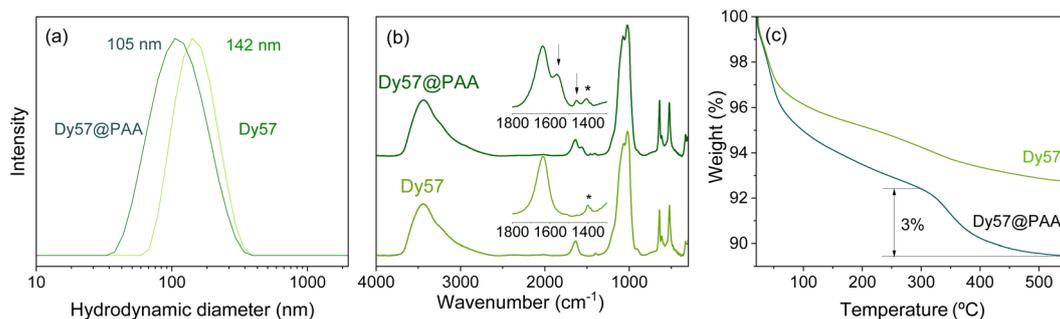
Fig. 3 (a) DLS size distribution curve in water, (b) FTIR spectra, and (c) thermogravimetry curves of Dy57NPs and Dy57@PAA NPs. Insets in (b) are magnifications of selected regions for clarity.

NPs showed, in addition to both weight losses, a steeper loss of around 4% at ∼300 °C that can be due to the decomposition of PAA entities. Similar TG curves were observed for Dy23 and Dy37 before and after functionalization (Fig. S4†). The FTIR and TG results demonstrate, therefore, that all three types of NPs were successfully coated with PAA. The colloidal stability of the functionalized NPs suspended in water (native pH ∼ 7.0) was then re-evaluated using DLS. The DLS curves of the functionalized NPs suspended in water significantly shifted towards lower hydrodynamic values with respect to those recorded before functionalization, as observed in Fig. 3a for Dy57@PAA NPs and in Fig. S2† for Dy23@PAA and Dy37@PAA. It can be therefore concluded that the functionalization process notably improved the colloidal stability of the NPs in water. However, all three types of NPs showed a certain degree of aggregation, as inferred from the higher values of their hydrodynamic size in water (86 nm, 85 nm and 105 nm for Dy23, Dy37, and Dy57 NPs, respectively) compared with their TEM size.

Finally, the PAA-functionalized NPs were suspended in PBS (pH = 7.4) to assess their colloidal stability in a buffer solution commonly used in biological research to simulate physiological fluid. All three NPs functionalized with PAA could be easily re-dispersed in the buffer, as demonstrated by the DLS curves shown in Fig. 4, with hydrodynamic sizes similar to those in water (between 80 nm and 100 nm).
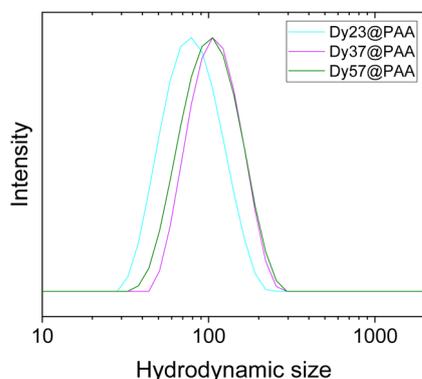

Fig. 4 DLS curves of Dy23@PAA, Dy37@PAA, and Dy57@PAA NPs suspended in PBS.

Finally, in order to analyze the chemical stability of DyPO$_4$ NPs in physiological medium, we have selected the Dy57@PAA NPs as a proof of concept and studied their possible dissolution with time in PBS suspension (pH = 7.4) at 37 °C (physiological temperature). The value of Dy fraction dissolved after 1, 3, and 5 weeks of incubation was 0.15%, 0.10%, and 0.72%, respectively, which indicates a negligible degree of dissolution of DyPO$_4$ in PBS. This value was, in addition, significantly lower than those reported for fluoride-based NPs (NaYF$_4$ and KYF$_4$) incubated in the same conditions for just 3 days, which showed 30% and 45%, respectively, of fluorine dissolved.[23] In conclusion, DyPO$_4$ NPs show an excellent degree of chemical stability under simulated physiological conditions.

2.3. Relaxivity study

The performance of the three different NPs@PAA as UHF MRI contrast agents was evaluated using a preclinical 9.4 T MRI scanner at room temperature (RT, 23 °C). Fig. 5a shows the T_2-weighted MR images obtained in aqueous suspensions with different concentrations of Dy23@PAA, Dy37@PAA, and Dy57@PAA NPs. The images became darker as the NPs concentration increased for all three samples, and they turned practically black at concentrations as low as ∼0.3 mM Dy, which indicates that the NPs behaved as excellent negative MRI CAs. The inverse of the experimentally determined transverse relaxation rates ($1/T_2$) of water protons was plotted against the molar concentration of Dy^{3+} in the aqueous suspensions (Fig. 5b). The r_2 values, determined from the slope of the fitted line, were as high as 395, 432, and 516 mM^{-1} s^{-1} for Dy23@PAA, Dy37@PAA, and Dy57@PAA NPs, respectively. The r_2 values increased, therefore, with increasing particle size. This trend agrees well with the literature for other nanoparticulated systems such as HoF$_3$,[16] NaHoF$_4$,[30] NaDyF$_4$,[17] Dy$_2$O$_3$,[18] and HoPO$_4$,[29] where an increase in transversal relaxivity was observed with increasing nanoparticle size. This effect is due to the dependence of the proton relaxation enhancement on spins correlation times, as explained in detail by Yung.[31] It is reported that NPs aggregation could also influence their MRI performance.[32] However, in our case, the Dy37 NPs clearly showed a higher r_2 value than the Dy23 NPs in spite of their very similar hydrodynamic diameters in water. Therefore, the
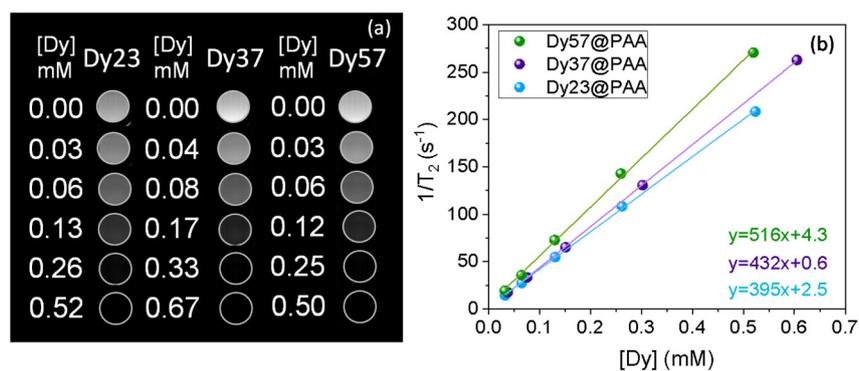
Fig. 5 (a) Concentration-dependent T_2 weighted phantom images of the Dy23@PAA, Dy37@PAA, and Dy57@PAA NPs at 9.4 T. (b) T_2 relaxation rates as a function of Dy concentration of Dy23@PAA, Dy37@PAA, and Dy57@PAA aqueous suspensions at 9.4 T.

r_2 values are governed by the core size. The relaxivity values reported for our DyPO$_4$@PAA NPs were, to the best of our knowledge, the highest r_2 values ever reported at 9.4 T for any Dy-based nanometric particles in the literature, such as DyF$_3$, NaDyF$_4$, or Dy$_2$O$_3$, which showed r_2 values between 100 and 380 mM^{-1} s^{-1}.[16–18] Sample Dy57@PAA, showing the highest r_2 value (516 mM^{-1} s^{-1}) among the three NPs of this study, was subsequently used for biocompatibility studies and for *in vivo* experiments.

2.4. Biocompatibility studies

Previous to biocompatibility studies, the Dy57@PAA NPs were coated with PEG, as described in the Experimental section, with the purpose of improving their systemic circulation time and avoiding their clearance by the immune system.[21] The NPs were successfully PEGylated, as demonstrated by the FTIR spectra shown in Fig. S5a.† Fig. S5b† shows the DLS curve of the corresponding NPs suspended in PBS, exhibiting a hydrodynamic size of 164 nm. The PEGylated sample was submitted as well to magnetic resonance studies, obtaining a value for r_2 of 438 mM^{-1} s^{-1}, slightly lower than that of the NPs before PEGylation (516 mM^{-1} s^{-1}) (Fig. S5c†). The surface coating is an important factor that influences transversal relaxivity. In general, according to a quantum mechanical outer-sphere theory, r_2 decreases with increasing the thickness of the surface coating.[33] In our case, the PEGylated sample, with a thicker coating than the non-PEGylated nanoparticles (just coated with PAA), gave a lower r_2 value than the latter, in agree-
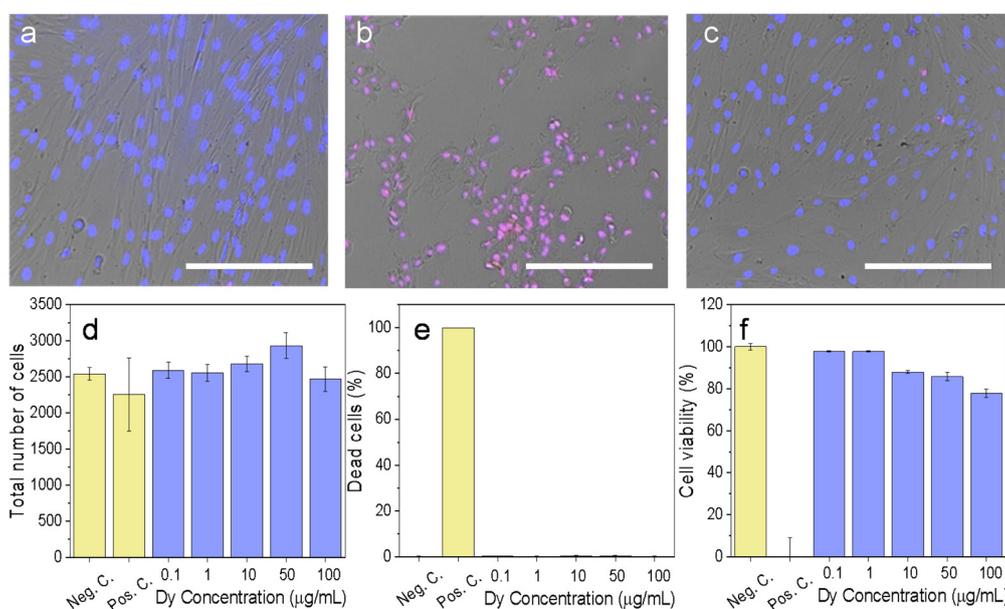

Fig. 6 Optical microscopy images of HFF-1 fibroblasts resulting from the merge of bright field (grey), Hoechst 33342 (blue) and TO-PRO-3 Iodine (red) images: (a) negative control, (b) positive control, (c) cells exposed to 100 µg ml^{-1} of Dy57@PAA@PEG NPs. Scale bar corresponds to 50 µm. (d) Total number of cells per well after exposure to increasing concentration of Dy57@PAA@PEG NPs. (e) Percentage of dead cells after exposure to increasing concentration of Dy57@PAA@PEG NPs. (f) MTT assay of cells exposed to increasing concentration of Dy57@PAA@PEG NPs.

ment with the theory. The corresponding phantom images also show a clear darkening with increasing NPs concentration (Fig. S5d†).

Biosafety studies of Dy57@PAA@PEG NPs were evaluated in HFF-1 human foreskin fibroblasts. Several parameters were examined to get a complete assessment of the cytotoxic behavior, such as cell morphology, induction of necrotic/late apoptotic cells, and mitochondrial activity. When merging bright-field, DNA staining (Hoechst 33342), and nuclei staining (TO-PRO-3 Iodine) to get microscopy images, it was found that cells exposed to a NPs concentration up to 100 µg mL^{-1}

(referred to Dy^{3+}), did not show any appreciable morphological change (Fig. 6a–c).

On the other hand, cellular necrosis and apoptosis were assessed in the "live-dead" assay. The total number of cells per well remained unaltered for all the NPs concentrations tested (Fig. 6d) while these NP concentrations did not give rise to a relevant increase in cell death, which remained very close to zero in all cases (Fig. 6e). Finally, no statistically significant effect on mitochondrial activity was observed with the MTT assay, which showed a cell survival close to 100% for NPs concentrations up to 100 µg mL^{-1} Dy (Fig. 6f). These results
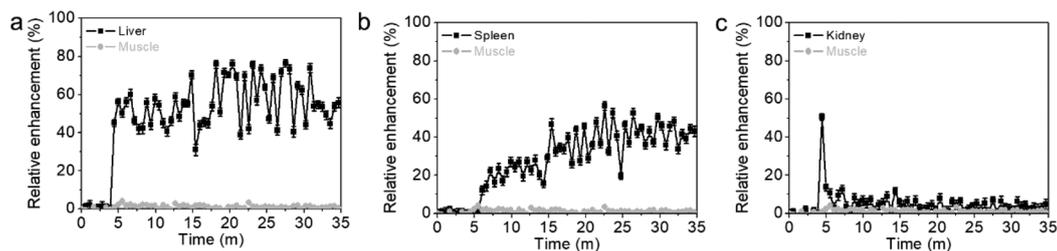

Fig. 7 Short-term pharmacokinetics of intravenously injected Dy57@PAA@PEG NPs (5 mg Dy kg^{-1} animal) determined by dynamic T_2-weighted MRI. (a) liver, (b) spleen, and (c) kidney. Muscle (grey) is plotted as a reference in all cases.
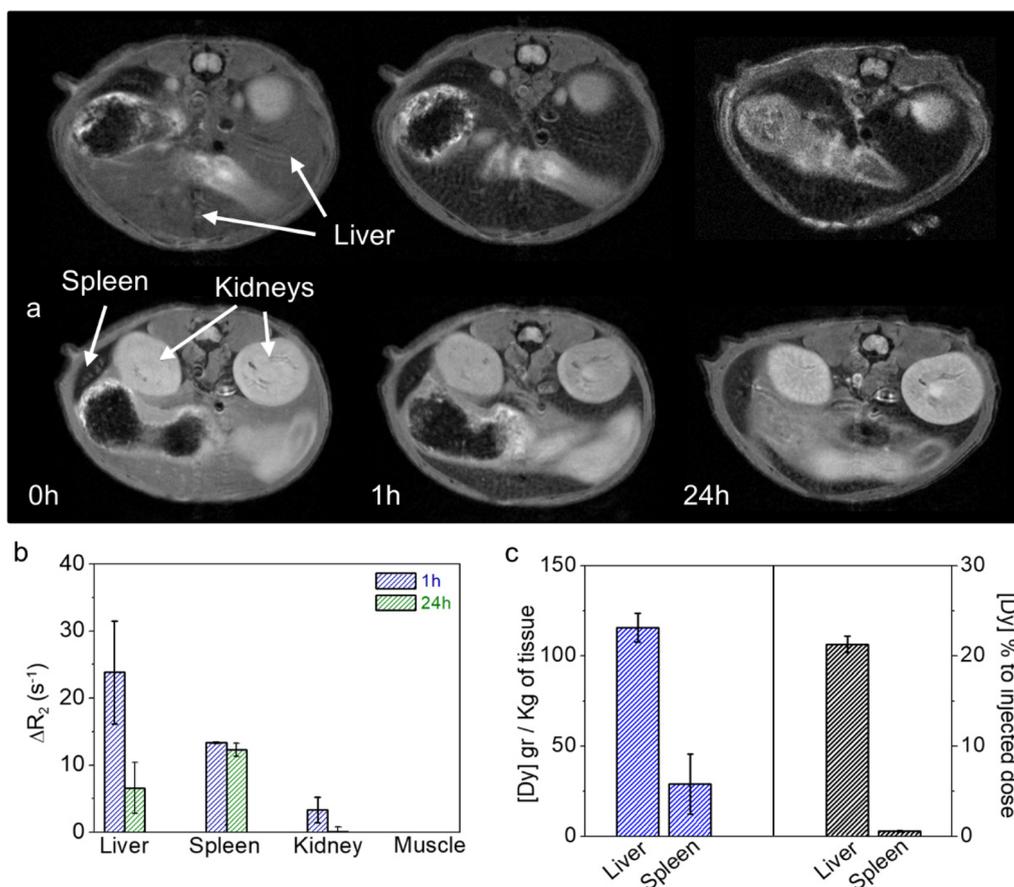

Fig. 8 Representative T_2-weighted MR images at different time points after the intravenous injection of Dy57@PAA@PEG NPs (5 mg Dy kg^{-1} animal) (a). ΔR_2 changes in liver, spleen, kidney, and muscle calculated from MRI T_2 maps at different time points (b). Absolute and relative concentrations of Dy (g Dy kg^{-1} of tissue and % to the injected dose) in liver and spleen at 24 h post-injection of NPs (c).
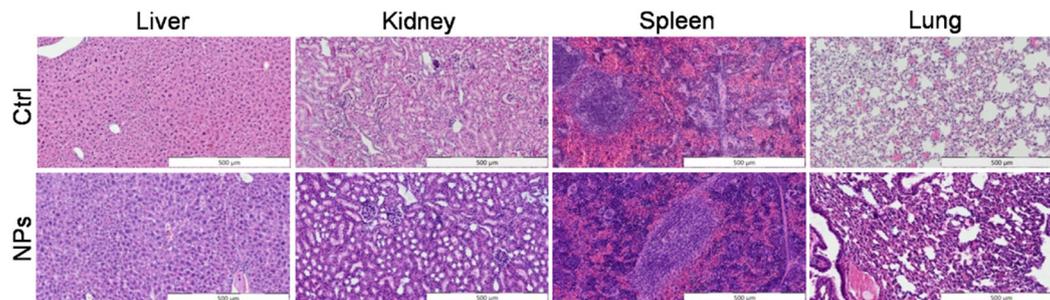
Fig. 9 H&E staining of tissue sections of liver, kidney, spleen, and lung injected with saline (Ctrl) and with Dy57@PAA@PEG NPs.

clearly indicate negligible toxicity effects under the assayed conditions and, therefore, the suitability of the DyPO$_4$ NPs as bioimaging probes.

2.5. *In vivo* studies

The *in vivo* behavior of intravenously injected Dy57@PAA@PEG NPs was assessed by dynamic T_2-weighted MRI and quantitative T_2 mapping. Dynamic MRI was used to obtain short-term pharmacokinetics (Fig. 7), which revealed fast liver and spleen uptake, while no accumulation was observed in the kidneys. Interestingly, liver uptake was notably higher and faster than splenic uptake, agreeing with uptake pharmacokinetics reported for PEGylated iron oxide NPs in the same size range.[34] This behavior can be explained by a higher endocytic/phagocytic affinity for nanomaterials from Kupffer cells compared to splenic macrophages, as reported by Tsoi *et al.*[35]

Additionally, long-term pharmacokinetics, up to 24 h, were also studied by quantitative T_2 mapping. As expected, a drastic T_2 decay (or R_2 increase) was observed in the liver and spleen 1 hour after the injection of Dy57@PAA@PEG NPs, with ΔR_2 of 24 s^{-1} and 14 s^{-1}, respectively (Fig. 8a and b). At 24 h, a considerable number of NPs was still retained in the liver, as evidenced by its low T_2 values ($\Delta R_2 = 6.6$ s^{-1}, while T_2 values in the spleen were almost the same as after 1 hour ($\Delta R_2 = 12.3$ s^{-1}). These quantitative results agree well with the short-term pharmacokinetics discussed above, showing higher uptake/affinity of NPs by the liver. Post-mortem quantification of Dy57@PAA@PEG NPs content in tissue extracts by ICP-MS (Fig. 8c) showed high concentrations of Dy in the liver (115 g Dy kg^{-1} of tissue) and much lower in the spleen (29 g Dy kg^{-1} of tissue), which corresponded to ≈23% and ≈0.6% respect of the injected dose, respectively. This result might seem controversial with the MRI data; they could be explained by the total or partial degradation of NPs in the liver, leading to a decay in the R_2 values, even with a high concentration of Dy in the tissue, while much less NPs degradation occurred in the spleen. Therefore, hepatobiliary elimination, which has been proclaimed as one of the main mechanisms of removing NPs from the bloodstream,[36] can be described as the main excretion pathway for these NPs.

As for the kidneys, a slight T_2 decay ($\Delta R_2 = 4$ s^{-1}) was observed 1 h after NPs injection, which can be attributed to the passage of the remaining NPs in the bloodstream. As expected, kidney T_2 values returned to normality at 24 hours, consistent with the absence of NPs in the bloodstream at that time.

Finally, tissue sections of the main organs were analyzed histologically to assess the *in vivo* toxicity of Dy57@PAA@PEG NPs (Fig. 9). All organs analyzed, including liver, kidney, spleen, and lung, exhibited normal cytoarchitecture, comparable to controls (injected with saline), with no observable histopathological changes, such as necrosis or inflammatory cell infiltrations, indicative of tissue damage.[37] These findings provide further evidence of the biocompatibility of Dy57@PAA@PEG NPs.

3. Conclusions

DyPO$_4$ nanoparticles were synthesized using a homogeneous precipitation method in butanol at 150 °C from dysprosium nitrate and phosphoric acid in a microwave oven. NPs size could be tuned from 23 nm to 57 m by varying the phosphoric acid concentration in the starting solution. The experimental conditions that were found necessary to synthesize uniform NPs were quite restrictive, as their variation gave rise to either heterogeneous or aggregated NPs. After functionalization with PAA, the NPs showed good colloidal stability in both water and PBS suspensions. The high chemical stability was also checked in a simulator of physiological medium; the NPs remained unaltered after five weeks at 37 °C. Transversal relaxivity values (r_2) of 395, 432, and 516 mM^{-1} s^{-1} were found for the 23, 37, and 57 nm sized NPs at 9.4 T, the latter being the highest r_2 value ever reported for Dy-based NPs at that magnetic field. The biocompatibility of the PEG-functionalized NPs was assessed, exhibiting negligible toxicity effects. Moreover, pharmacokinetic assays indicated faster liver than spleen uptake, while no accumulation was observed in the kidneys. Finally, histological studies showed no tissue damage in any of the studied organs, providing further evidence on the biocompatibility of DyPO$_4$ NPs and, therefore, their suitability as bioimaging probes.

4. Experimental section

4.1. Reagents

Dysprosium nitrate hydrate (Dy(NO$_3$)$_3$·5H$_2$O, Sigma Aldrich, 99.99%), phosphoric acid (Sigma Aldrich, 85%), butanol

(Sigma Aldrich, >99.5%), and 1-octanol (Merck, >99%) were used for NPs synthesis. Poly(acrylic acid) (PAA, average $M_w \sim$ 1800, Sigma-Aldrich) was used for NPs functionalization with PAA. For NPs functionalization with PEG, the following reagents were used as received: 1-(3-dimethylaminopropyl)-3-ethyl carbodiimide (EDC – Sigma Aldrich, USA), N-hydroxysulfosuccinimide (s-NHS -Sigma Aldrich, USA) and α-methoxy-ω-amino PEG of 5000 Da (PEG, RappPolymer, Germany). Colloidal stability of NPs was evaluated using an aqueous solution of Phosphate Buffered Saline (PBS, Sigma Aldrich) that was prepared as follows: one tablet of PBS was dissolved in 200 mL water to obtain 137 mM NaCl, 2.7 mM KCl and 10 mM phosphate buffer, pH 7.4 at 25 °C. An aqueous solution of sodium tetraborate decahydrate (Sigma Aldrich, >99.5%) 10 mM was prepared and its pH was adjusted to 9 with NaOH. We call this solution borate buffer from now on.

4.2. NPs synthesis

For the synthesis of uniform dysprosium phosphate nanoparticles, we used a homogeneous precipitation reaction. Essentially, the method consists of aging a mixture of Dy(NO$_3$)$_3$ with phosphoric acid in butanol at 150 °C in a microwave oven (Sineo MDS-8, Microwave Chemistry Workstation). The standard procedure is as follows: dysprosium nitrate was dissolved in 30 mL of butanol at 50 °C for 1 h under magnetic stirring to facilitate dissolution in order to get a 0.02 M dysprosium nitrate solution. Once dissolved, the solution was admixed with 616 microliters of H$_3$PO$_4$ to obtain a final solution with 0.30 M H$_3$PO$_4$ concentration. The mixture was aged in tightly closed test tubes using a microwave oven at 150 °C for 1 h. The resulting dispersion was cooled down to RT, centrifuged to remove the supernatants, and washed twice with ethanol and once with double distilled water. The NPs were finally stored either in distilled water or dried at 50 °C for some analyses. Additional experiments were conducted to analyze the effect of synthesis parameters (solvent nature, H$_3$PO$_4$ concentration, aging temperature, and heating source) on the characteristics of the precipitated nanoparticles.

4.3. NPs functionalization

Functionalization with PAA. The aqueous suspension of NPs obtained as described above was diluted in Milli-Q water to get a concentration of 1 mg mL^{-1} and its pH was adjusted to 10 with 1 M NaOH solution. PAA (2 mg mL^{-1}) was then added to the suspension and, again, the pH was adjusted to 10. The resulting suspension was magnetically stirred for 1 h at RT and centrifuged at 14000 rpm for 20 min to remove the supernatant. The resulting NPs were washed twice with Milli-Q water through centrifugation in the same conditions and stored in Milli-Q water. The pH of the resultant suspension was close to 7.

Functionalization with α-methoxy-ω-amino PEG (PEG). The NPs showing the optimum magnetic relaxivity value in this study were further functionalized with PEG. For PEG coating, the NPs were firstly functionalized with PAA following the same procedure described above but using 10 mg mL^{-1} PAA to increase the number of carboxylate groups on the NPs surface for PEG grafting. The obtained NPs were then suspended in borate buffer (6 mg NPs mL^{-1}). A volume of 0.94 mL of an EDC solution in borate buffer (3.2 mg mL^{-1}) was admixed with 0.85 mL of s-NHS solution in borate buffer (6 mg mL^{-1}).[38] The mixture was shaken at RT for 10 min in the end-over-end roller. A volume of 161 µl of the NPs@10PAA suspension was added to the resulting solution. The three mentioned volumes were chosen in order to get the following molar ratio: 1 COOH : 10 EDC : 15 NHS (COOH refers to the carboxylic groups in PAA attached to the NPs). The resultant suspension was stirred at RT for 2 h in the end-over-end roller and admixed with 1.56 ml of a PEG solution in borate buffer (10 mg mL^{-1}) (in accordance with the ratio 1 COOH : 2 PEG). Finally, after 45 minutes of stirring at RT in the end-over-end roller, NPs were separated by centrifugation at 14 500 rpm for 5 minutes. The resulting NPs were washed twice with borate buffer and they were suspended in 1 mL of fresh borate buffer and stored at 4 °C. This protocol was repeated ten times to have enough NPs for the rest of the analyses.

4.4. Chemical stability studies

NPs functionalized with PAA were suspended in PBS (pH = 7.4) and the suspension was magnetically stirred at 37 °C for several weeks. A portion of the suspension was extracted and centrifuged after 1, 3, and 5 weeks and the supernatants were analyzed by ICP to determine the fraction of dissolved dysprosium.

4.5. Characterization techniques

Transmission electron microscopy (TEM, JEOL 2100Plus) was used to determine particles shape and size. To prepare the sample for the TEM analyses, a droplet of the NPs aqueous suspension was deposited on a copper grid coated with a transparent polymer. Particle size distribution curves were obtained by counting about one hundred of particles on the TEM micrographs using the ImageJ open-source image processing program.

The colloidal stability of the NPs before and after functionalization was assessed by Dynamic Light Scattering (DLS, Malvern Zetasizer Nano-ZS90). DLS curves were obtained both in aqueous and PBS suspensions with ~0.5 mg NPs mL^{-1}.

Ion Coupling Plasma (ICP) analyses of NPs were carried out in an iCAP 7200 ICP-OES Duo (ThermoFisher Scientific) apparatus. ICP analyses on tissues were carried using a PerkinElmer NexION installed at the Central Research Services (University of Malaga, Spain). Tissue samples digestion was performed in a microwave digestion system (Milestone). In brief, 0.1 mg of tissue was digested with 6 mL of nitric acid at 240 °C and 40 bar for 50 min. Then, Milli-Q water was added up to 25 mL.

X-ray powder diffraction (XRD) was used for phase identification. The XRD patterns were recorded with a Panalytical X'Pert Pro diffractometer (Cu Kα) with an X-Celerator detector in the angular range of 10° < 2θ < 80° using a 2θ step width of 0.02° and 10 s counting time. The crystallite size was estimated

using the Scherrer formula from the full width at half maximum (FWHM) of a single reflection. A shape factor of $k = 0.9$ and an instrumental broadening factor of 0.112 were used for the calculation.

The success of the functionalization processes was proved using Fourier Transform Infrared (FTIR) spectroscopy and Thermogravimetric analyses (TGA). FTIR (Jasco FT/IR-6200) was conducted on NPs pellets diluted in KBr while TGA curves were recorded in a Q600TA Instrument at a heating rate of $10\ °C\ min^{-1}$ in air.

4.6. Magnetic relaxivity

Transverse magnetic relaxivity (r_2) was measured at 1.44 T on a Bruker Minispec (TD-NMR) system and at 9.4 T on a Bruker Biospec MRI system. T_2 values were determined in aqueous suspensions of NPs with concentrations of Dy ranging from 0.01 to 0.70 mM, using spectroscopic or imaging sequences based on the Carl-Purcell-Meiboom-Gill (CPMG) scheme. r_2 values were obtained from the slope of the linear fit of $1/T_2$ to the concentration of Dy expressed in mM.

4.7. Cytotoxicity

Cytotoxicity was determined in human fibroblasts (HFF-1) using Live–Dead and MTT assays. Fibroblasts were used in this work with the purpose of testing unspecific cytotoxicity in normal cells. The Live–Dead assay was evaluated on a PerkinElmer Operetta High Content Imaging System. Cell viability markers to study mitochondrial activity, cell morphology, and plasma membrane integrity, were assessed in HFF-1 following the protocols described previously by some of us.[39]

4.8. *In vivo* MRI

All animal studies were performed complying with the Spanish and European Guidelines for Care and Use of Laboratory Animals (R.D. 53/2013 and 2010/62/UE) and approved by the Local Animal Ethics Committee and the Highest Institutional Ethics Committee (Andalusian Government, accreditation number 14/09/2021/130).

Mice were anesthetized with isoflurane (0.5–1% in oxygen at $1\ L\ min^{-1}$) and their tail vein cannulated for NPs administration. Then, mice were placed in the magnet, where the vital constants, respiration, and body temperature, were monitored throughout the experiment. NPs were administered intravenously at a concentration of $5\ mg\ Dy\ kg^{-1}$ animal, which was enough to observe a good contrast.

MR images were acquired on the Bruker Biospec 9.4 T system mentioned above, equipped with a 40 mm quadrature bird-cage resonator. Both acquisition and image analysis were conducted as previously described elsewhere.[40] The acquisition scheme consisted of high-resolution T_2-weighted images, T_2 parametric images (quantitative), intravenous injection of the NPs, dynamic T_2-weighted sequence, and again high-resolution and parametric T_2 images. High-resolution T_2-weighted images were acquired using a turbo-RARE sequence with respiratory gating (TE = 16 ms, TR = 1000 ms, 4 averages, FOV = 4 cm, matrix size = 384 × 384, slice thickness = 1 mm).

T_2 maps were acquired using a multi-echo spin-echo sequence (TEs ranging from 7 ms to 448 ms, TR = 3500 ms, FOV = 4 cm, matrix size = 128 × 128, slice thickness = 1 mm). Short-term pharmacokinetics (first 30 min) were obtained from the semi-quantitative analysis of the dynamic T_2-weighted sequence. Quantitative T_2 images were acquired at 0, 1, and 24 h to assess the long-term pharmacokinetics and biodistribution of NPs. After 24 h of NPs injection, mice were sacrificed and tissue samples collected for histological evaluation and quantification of the Dy content.

4.9. Histology

Kidney, spleen, and liver tissue sections were stained with Haematoxylin and Eosin (H&E) to assess tissue architecture by light microscopy. The tissues were fixed in 4% formaldehyde (Panreac, pH 7 buffered) for 48 h, changing the 4% formaldehyde after 24 h. Then, the samples were dehydrated through graded ethanol, and embedded in paraffin (temperature 56° C for 2 h under stirring and vacuum). The detailed procedures are described below. Haematoxylin and Eosin (H&E): paraffin-embedded samples were sectioned at 7 μm thickness, then deparaffinized, rehydrated, and stained with H&E, and then dehydrated in ascending concentrations of ethanol, cleared in xylene, and mounted on commercial glass slides.

Conflicts of interest

The authors declare that they have no known competing financial interests or personal relationships that could have appeared to influence the work reported in this paper.

Acknowledgements

References

1 J. H. Duyn, *NeuroImage*, 2012, **62**, 1241–1248.

2 H. K. Kim, A. R. Baek, G. Choi, J. J. Lee, J. U. Yang, H. Jung, T. Lee, D. Kim, M. Kim, A. E. Cho, G. H. Lee and Y. Chang, *Biomaterials*, 2020, **243**, 119939.

3 T. Vaughan, L. DelaBarre, C. Snyder, J. F. Tian, C. Akgun, D. Shrivastava, W. Z. Liu, C. Olson, G. Adriany, J. Strupp, P. Andersen, A. Gopinath, P. F. van de Moortele, M. Garwood and K. Ugurbil, *Magn. Reson. Med.*, 2006, **56**, 1274–1282.

4 N. J. Shah, *Brain Struct. Funct.*, 2015, **220**, 1867–1884.

5 X. F. Tian, D. M. Wang, S. Feng, L. Zhang, X. M. Ji, Z. Wang, Q. Y. Lu, C. Y. Xi, L. Pi and X. Zhang, *NeuroImage*, 2019, **199**, 273–280.

6 M. Harris, S. Biju and T. N. Parac-Vogt, *Chem. – Eur. J.*, 2019, **25**, 13838–13847.

7 P. Caravan, *Chem. Soc. Rev.*, 2006, **35**, 512–523.

8 A. Gautam, P. Komal and R. S. Singh, *J. Chem. Sci.*, 2019, **131**.

9 A. Banerjee, B. Blasiak, A. Dash, B. Tomanek, F. C. J. M. van Veggel and S. Trudel, *Chem. Phys. Rev.*, 2022, **3**, 011304.

10 B. M. Alsaadi, F. J. C. Rossotti and R. J. P. Williams, *J. Chem. Soc., Dalton Trans.*, 1980, 2147–2150.

11 G. Pintacuda, M. John, X. C. Su and G. Otting, *Acc. Chem. Res.*, 2007, **40**, 206–212.

12 S. Aime, M. Botta, L. Barbero, F. Uggeri and F. Fedeli, *Magn. Reson. Chem.*, 1991, **29**, S85–S88.

13 P. Caravan, M. T. Greenfield and J. W. M. Bulte, *Magn. Reson. Med.*, 2001, **46**, 917–922.

14 M. Harris, C. Henoumont, W. Peeters, S. Toyouchi, L. Vander Elst and T. N. Parac-Vogt, *Dalton Trans.*, 2018, **47**, 10646–10653.

15 X. Y. Zheng, J. Pellico, A. A. Khrapitchev, N. R. Sibson and J. J. Davis, *Nanoscale*, 2018, **10**, 21041–21045.

16 A. Baek, H. K. Kim, J. U. Yang, G. Choi, M. Kim, A. E. Cho, Y. H. Kim, S. Kim, B. Sung, B. W. Yang, H. Seo, G. H. Lee, H. K. Ryeom, H. Jung, T. Lee and Y. Chang, *J. Ind. Eng. Chem.*, 2020, **85**, 297–307.

17 D. Gonzalez-Mancebo, A. I. Becerro, T. C. Rojas, M. L. Garcia-Martin, J. M. de la Fuente and M. Ocana, *Part. Part. Syst. Charact.*, 2017, **34**, 1700116.

18 G. K. Das, N. J. J. Johnson, J. Cramen, B. Blasiak, P. Latta, B. Tomanek and F. van Veggel, *J. Phys. Chem. Lett.*, 2012, **3**, 524–529.

19 M. Norek, E. Kampert, U. Zeitler and J. A. Peters, *J. Am. Chem. Soc.*, 2008, **130**, 5335–5340.

20 Y. Li, Y. Y. Gu, W. Yuan, T. Y. Cao, K. Li, S. P. Yang, Z. G. Zhou and F. Y. Li, *ACS Appl. Mater. Interfaces*, 2016, **8**, 19208–19216.

21 B. Pelaz, P. del Pino, P. Maffre, R. Hartmann, M. Gallego, S. Rivera-Fernandez, J. M. de la Fuente, G. U. Nienhaus and W. J. Parak, *ACS Nano*, 2015, **9**, 6996–7008.

22 J. Nam, N. Won, J. Bang, H. Jin, J. Park, S. Jung, Y. Park and S. Kim, *Adv. Drug Delivery Rev.*, 2013, **65**, 622–648.

23 D. Lisjak, O. Plohl, J. Vidmar, B. Majaron and M. Ponikvar-Svet, *Langmuir*, 2016, **32**, 8222–8229.

24 M. I. Saleh, B. Ruhle, S. Wang, J. Radnik, Y. You and U. Resch-Genger, *Sci. Rep.*, 2020, **10**, 19318.

25 F. H. Firsching and S. N. Brune, *J. Chem. Eng. Data*, 1991, **36**, 93–95.

26 R. Meenambal, P. Poojar, S. Geethanath and K. Sanjeevi, *J. Am. Ceram. Soc.*, 2017, **100**, 1831–1841.

27 V. K. Lamer and R. H. Dinegar, *J. Am. Chem. Soc.*, 1950, **72**, 4847–4854.

28 Y. Gao, M. Fan, Q. Fang, B. Song and W. Jiang, *J. Nanosci. Nanotechnol.*, 2013, **13**, 6644–6652.

29 A. I. Becerro and M. Ocana, *RSC Adv.*, 2015, **5**, 34517–34524.

30 D. L. Ni, J. W. Zhang, W. B. Bu, C. Zhang, Z. W. Yao, H. Y. Xing, J. Wang, F. Duan, Y. Y. Liu, W. P. Fan, X. Y. Feng and J. L. Shi, *Biomaterials*, 2016, **76**, 218–225.

31 K. T. Yung, *Magn. Reson. Imaging*, 2003, **21**, 451–463.

32 H. T. Ta, Z. Li, Y. Wu, G. Cowin, S. Zhang, A. Yago, A. K. Whittaker and Z. P. Xu, *Mater. Res. Express*, 2017, **4**, 116105.

33 W. Zhang, L. Liu, H. Chen, K. Hu, I. Delahunty, S. Gao and J. Xie, *Theranostics*, 2018, **8**, 2521–2548.

34 M. Pernia Leal, C. Caro and M. L. García-Martín, *Nanoscale*, 2017, **9**, 8176–8184.

35 K. M. Tsoi, S. A. MacParland, X.-Z. Ma, V. N. Spetzler, J. Echeverri, B. Ouyang, S. M. Fadel, E. A. Sykes, N. Goldaracena, J. M. Kaths, J. B. Conneely, B. A. Alman, M. Selzner, M. A. Ostrowski, O. A. Adeyi, A. Zilman, I. D. McGilvray and W. C. W. Chan, *Nat. Mater.*, 2016, **15**, 1212–1221.

36 W. Poon, Y.-N. Zhang, B. Ouyang, B. R. Kingston, J. L. Y. Wu, S. Wilhelm and W. C. W. Chan, *ACS Nano*, 2019, **13**, 5785–5798.

37 K. E. Ibrahim, M. G. Al-Mutary, A. O. Bakhiet and H. A. Khan, *Molecules*, 2018, **23**, 1848.

38 Z. Grabarek and J. Gergely, *Biophys. J.*, 1988, **53**, A392.

39 E. Gomez-Gonzalez, C. Caro, D. Martinez-Gutierrez, M. L. Garcia-Martin, M. Ocana and A. I. Becerro, *J. Colloid Interface Sci.*, 2021, **587**, 131–140.

40 C. Caro, M. C. Muñoz-Hernandez, M. Pernia Leal and M. L. García-Martín, *Preclinical Mri: Methods and Protocols*, 2018, vol. 1718, pp. 409–419.